Strain-Induced Medium-Temperature Thermoelectric Performance of Cu₄TiSe₄: The Role of Four-Phonon Scattering

Xue-Kun Chen [1,*] En-Ming Zhang,[1] Dan Wu [2,†] and Ke-Qiu Chen [3,‡]

[1]*School of Mathematics and Physics, University of South China, Hengyang 421001, People's Republic of China*
[2]*School of Physics and Electronic Science, Changsha University of Science and Technology, Changsha 410114, China*
[3]*Department of Applied Physics, School of Physics and Electronics, Hunan University, Changsha 410082, China*

Motivated by the synthesized Cu₄TiSe₄ with ultralow room-temperature thermal conductivity [Angew. Chem., Int. Ed. 60, 9106 (2021)], we systematically investigate its thermoelectric (TE) properties via combining Boltzmann transport equations and first-principles calculations. The results show that the thermal conductivity of Cu₄TiSe₄ determined considering only three-phonon scattering is reduced by about 40% after including four-phonon scattering at room temperature, indicating the importance of four-phonon scattering in phonon transport. On the other hand, the coexistence of high dispersion and valley degeneracy at the top valence band in the electronic structure causes a high power factor. Consequently, the isotropic figure of merit (ZT) value of 1.5 at 500 K is captured in the p-type doped Cu₄TiSe₄. In addition, the value of ZT can be further enhanced to 2.2 by applying 2.25% triaxial tensile strain, which is ascribed to the remarkably enhanced four-phonon scattering processes induced by the tensile strain. Meanwhile, the significant suppression of thermal conductivity allows the optimal carrier concentration for the ZT peak to be reduced, which is of important practical significance for the experimental preparation of Cu₄TiSe₄-based TE devices. Our results pave a way for the design of adjustable medium-temperature TE devices.

I. INTRODUCTION

In the background of the global energy crisis and CO_2 emission reduction, the demands for clean and sustainable power have greatly renewed attention in thermoelectric (TE) materials, which allow direct mutual conversion between low-grade heat and electrical energy by the Seebeck effect [1]. TE materials have long been designed to realize power generation and cool equipment without any movable components and have shown definite advantages in multiple applications such as radioisotope TE generators, temperature sensors, wearable devices, and car refrigerators [2]. At present, the major impediment that constrains the application of TE materials is the low conversion efficiency, especially at room to medium temperature. Hence, searching for highly efficient TE materials is the focus of research. Normally, the conversion efficiency of TE materials is evaluated by the dimensionless figure of merit $ZT = TS\sigma^2/(\kappa_e + \kappa_l)$, where S, σ, and T are the Seebeck coefficient, electrical conductivity, and absolute temperature, respectively. Here, the electronic thermal conductivity (κ_e) and lattice thermal conductivity (κ_l) together comprise the total thermal conductivity (κ). Clearly, a TE material with high ZT value requires a large power factor ($S\sigma^2$) and low κ. However, S, σ, and κ_e are intrinsically coupled via the carrier concentration (n) at a given temperature, resulting in a great challenge for significant improvements in ZT value. In order to optimize and balance these electronic transport parameters, several effective approaches have been proposed to achieve high ZT in recent decades, including band-structure engineering [3,4], microstructure manipulations [5–7], and reducing dimensionality [8–10]. On the other hand, the discovery of crystalline structures with intrinsically low κ_l characterized by resonant bonding [11], lone-pair electrons [12,13], and rattling [14,15] is an important strategy to obtain excellent TE performance. In addition, the manipulation of phonon transport to further reduce κ_l by introducing phonon interference/local resonance based on constructing superlattices/branched structures [16–18] or by enhancing phonon scattering based on defect engineering [19,20] and applying strain [9,21,22] is an extension of this strategy.

With the persistent efforts of researchers, various TE materials with relatively high ZT values have been proposed. For instance, a maximum ZT of 1.4 has been reported in Na-doped PbTe at 750 K because of a

*813112490@qq.com
†danwu@csust.edu.cn
‡keqiuchen@hnu.edu.cn

significant rise in the density of states around the Fermi level [23]. Later on, Tan *et al.* found a higher *ZT* of approximately 2.5 in a heavily alloyed PbTe-SrTe sample at 923 K because SrTe alloying of PbTe could cause valence-band convergence, strengthen phonon scattering, and improve extensive nanostructuring with good valence-band alignment of precipitate/matrix [24]. Moreover, Zhao *et al.* experimentally demonstrated that SnSe single crystals possess exceptionally low lattice thermal conductivity (0.23 Wm^{-1} K^{-1}) and a high *ZT* value (2.6) along the *b* axis at 923 K [25]. It is worth noting that the achievement of excellent TE performance in most of the previous studies depends on relatively high temperature (>700 K) [22,26–28]. Actually, a large amount of low-grade waste heat is stored at medium temperatures (around 500 K). Hence, the development of medium-temperature bulk TE materials with excellent performance becomes a major concern in the renewable energy field [29–31]. In theory, Yue *et al.* recently proposed host-guest structures like K_2Se_2 and Rb_2Se_2 with anisotropic bonding for capturing ultralow κ_l, and *ZT* values were predicted to be 2.95 for K_2Se_2 and 2.17 for Rb_2Se_2 along the *c* axis, respectively [32]. Wang *et al.* reported that, owing to the ultralow κ_l and the electronic band degeneracy/pockets near the Fermi level, a high $ZT > 3$ has been obtained in *n*-type doped Ba_2AgSb at 500 K [33]. In recent years, Cu-based compounds have attracted considerable attention as promising medium-temperature TE materials because of their nontoxicity and earth abundance [34]. In particular, Cu_2Se has been proven to possess electron-crystal and phonon-liquid behaviors, and the estimated *ZT* value could reach approximately 0.9 at 580 K [35]. With Al and Sn doping, the peak *ZT* could be further enhanced for the TE system. Very recently, the ternary copper-based chalcogenide compound Cu_4TiSe_4 has been synthesized by a high-temperature solid-state synthesis technique, and the crystal structure has also been characterized based on single-crystal x-ray diffractometry [36]. Moreover, it is found that Cu_4TiSe_4 possesses a moderate band gap (around 1.2 eV) and ultralow lattice thermal conductivity (0.19 W m^{-1} K^{-1}) owing to strong optical-acoustic coupling with low cutoff frequency, and so is expected to provide a potential opportunity for designing high-efficiency medium-temperature TE devices.

Motivated by the experimentally reported inherent advantages of Cu_4TiSe_4, we systematically study its TE performance by combining the Boltzmann transport equation (BTE) approach with first-principles calculations in this work. Our main finding is that four-phonon scattering significantly influences the lattice thermal conductivity of Cu_4TiSe_4 even at room temperature. On the other hand, the coexistence of high dispersion and valley degeneracy at the top valence band in the electronic structure causes a high power factor (PF). Consequently, the isotropic *ZT* value of 1.5 at 500 K is captured in the

p-type doped Cu_4TiSe_4. In addition, the value of *ZT* can be further enhanced to 2.2 by applying 2.25% tensile strain, which is ascribed to the remarkably enhanced four-phonon scattering processes induced by triaxial tensile strain.

II. CALCULATION DETAILS

All first-principles calculations are carried out using the Vienna *ab initio* simulation package based on the projector augmented wave method [37]. The Perdew-Burke-Ernzerhof (PBE) functional within the generalized gradient approximation (GGA) is used as the exchange-correlation functional [38], and the effect of spin-orbit coupling (SOC) is explicitly taken into account. The cutoff energy for the wave function is set to 600 eV. To ensure the convergence and rationality of the structural optimization, Brillouin zone (BZ) sampling is performed by a $21 \times 21 \times 21$ Γ-center mesh, and the convergence thresholds for electronic step and residual force are 10^{-8} eV and 10^{-4} eV Å^{-1}, respectively. Bonn effective charges and dielectric tensors needed for revising the dynamic matrix are also considered on the basis of density-functional perturbation theory [39].

For calculating the electronic transport properties, the BTE with the relaxation time approximation (RTA) in the framework of deformation potential theory is solved using the BOLTZ*ZT*RAP2 code [40] as libraries. The electrical conductivity σ, Seebeck coefficient *S*, and electronic thermal conductivity κ_e are calculated by the formula as follows:

$$\sigma = \frac{1}{\Omega N_{\mathbf{k}}} \sum_{v\mathbf{k}} (\tau_e v_e^2)_{v\mathbf{k}} \left(-\frac{\partial f}{\partial \varepsilon} \right)_{v\mathbf{k}}, \tag{1}$$

$$S = \frac{\sigma^{-1}}{\Omega N_{\mathbf{k}}} \sum_{v\mathbf{k}} (\tau_e v_e^2)_{v\mathbf{k}} (\varepsilon_{v\mathbf{k}} - \mu) \left(-\frac{\partial f}{\partial \varepsilon} \right)_{v\mathbf{k}}, \tag{2}$$

$$\kappa_e = \frac{1}{\Omega N_{\mathbf{k}} T} \sum_{v\mathbf{k}} (\tau_e v_e^2)_{v\mathbf{k}} (\varepsilon_{v\mathbf{k}} - \mu)^2 \left(-\frac{\partial f}{\partial \varepsilon} \right)_{v\mathbf{k}} - S^2 \sigma T, \tag{3}$$

where Ω, μ, and f denote volume, chemical potential, and Fermi-Dirac distribution function, respectively. τ_e and v_e are the relaxation time and group velocity at wave vector ($\mathbf{k}$) with band index v. Moreover, $N_{\mathbf{k}}$ is the number of *k*-point grids. Here, a dense $65 \times 65 \times 65$ *k*-point grid is used to capture the τ_e and other transport parameters. Since considering only electroacoustic phonon scattering could give rise to an overestimation of the *ZT* value for some semiconductors, such as PbTe and GaN [41,42], the impact of different scattering mechanisms is considered to calculate τ_e, namely,

$$\frac{1}{\tau_e} = \frac{1}{\tau_{\mathrm{ac}}} + \frac{1}{\tau_{\mathrm{imp}}} + \frac{1}{\tau_{\mathrm{pol}}}, \tag{4}$$

where τ_{ac}, τ_{imp}, and τ_{pol} represent the relaxation times of the electroacoustic phonon, electroimpurity, and electro-optical phonon scattering processes, respectively. The detailed expression of τ_{ac}, τ_{imp}, and τ_{pol} can be referred to in previous work, Ref. [43].

For calculating the phonon property and lattice thermal conductivity, the PHONOPY package [44] and the original and extended SHENGBTE packages [45,46] are applied to calculate harmonic (second-order) and anharmonic (third- and fourth-order) interatomic force constants (IFCs), respectively, based on the finite-displacement approach with a displacement of 0.01 Å. Specifically, to obtain the second-order IFCs, $3 \times 3 \times 3$ supercell and $7 \times 7 \times 7$ k-point meshes are used to compute the Hellmann-Feynman forces acting on each atom. Considering the balance of calculation accuracy and time, the cutoff is set to be the seventh nearest neighbors, fifth nearest neighbors, and third nearest neighbors for the second-order, the third-order, and fourth-order IFCs, respectively. Based on the iterative method, the κ_l tensor is written as

$$\kappa_l^{\alpha\beta} = \frac{1}{k_B T^2 \Omega N} \sum_{\mathbf{q}v} f_0(f_0+1)(\hbar\omega_{\mathbf{q}v})^2 v_{\mathbf{q}v}^{\alpha} F_{\mathbf{q}v}^{\beta}, \quad (5)$$

where k_B, f_0, $\hbar$, and $v_{\mathbf{q}v}$ are the Boltzmann constant, Bose-Einstein distribution, reduced Planck constant, and group velocity respectively. $F_{\mathbf{q}v} = \tau_{\mathbf{q}v}(v_{\mathbf{q}v} + \Delta_{\mathbf{q}v})$, $\tau_{\mathbf{q}v}$ is the phonon relaxation time obtained from the RTA method, and $\Delta_{\mathbf{q}v}$ denotes the correction of the deviation to the RTA prediction at wave vector $\mathbf{q}$ with band index v. Note that the Matthiessen's rule is utilized to estimate τ_p, which is written as

$$\frac{1}{\tau_p} = \frac{1}{\tau_{3ph}} + \frac{1}{\tau_{4ph}} + \frac{1}{\tau_{iso}}, \quad (6)$$

where τ_{3ph}, τ_{4ph}, and τ_{iso} represent the relaxation times of three-phonon, four-phonon, and isotope (iso) scattering processes, respectively. As suggested by previous work [46,47], the value of scalebroad is taken as 0.1. Here a carefully tested q mesh as large as $40 \times 40 \times 40$ ($14 \times 14 \times 14$

is adopted to ensure the convergence of κ_l considering three-phonon only (three- and four-phonon) scattering processes. The detailed convergence test for κ_l with respect to the q mesh can be found in Appendix A.

III. RESULTS AND DISCUSSION

A. Crystal structure, phonon dispersion, and electronic band structure

As suggested by Koley *et al.* [36], the disorder-free structure of Cu_4TiSe_4 contains nine atoms (four Cu, four Se, and one Ti) in the primitive cell with a cubic structure (the space group $P\bar{4}3m$), where the Cu atoms (Cu1 and Cu2) occupy the Wyckoff positions of 1a (0, 0, 0) and 3c (0.5, 0, 0.5), while the Se and Ti atoms are located in the 4e (0.23967, 0.23967, 0.23967) and 1b (0.5, 0.5, 0.5), respectively. Each Se atom could form tetrahedral coordination with a Ti atom and three Cu atoms. The distinct advantage of the crystal structure is that the influence of orientation on TE performance could be effectively eliminated. Figure 1(a) shows the top and side views of the bulk Cu_4TiSe_4. Here, the optimized lattice constant of Cu_4TiSe_4 is 5.67 Å. The calculated electronic band structures along the high-symmetry path Γ-X-M-Γ-R-X in the irreducible part of the BZ are presented in Fig. 1(b). It can be seen that an indirect band gap of 1.2 eV is presented between the M (valence band maximum, VBM) and [0.38, 0.0, 0.0] (conduction band minimum, CBM) points, which agrees well with the previously reported result [13]. Normally, the GGA PBE approximation underestimates the band gap, and the Heyd–Scuseria–Ernzerhof (HSE)06 approximation can be used for accurate band structure. Matyszczak *et al.* [48] have calculated the band gap of Cu_4TiSe_4 with the HSE06 approximation, and found that the obtained band structure profiles, except for the band gap (2.1 eV, indirect type), are very similar in the two applied approximations. Considering the band edge shape is more critical than the band gap itself for electronic transport [22,32,49], and the high computational cost of HSE06, the GGA PBE + SOC approximation is adopted
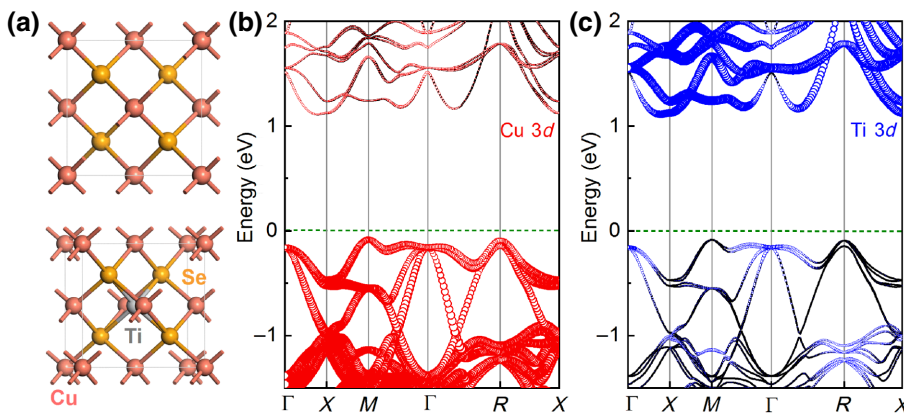

FIG. 1. (a) Top and side top view of geometric structure of Cu_4TiSe_4. Projected band structure of Cu_4TiSe_4 with (b) Cu 3d orbit and (c) Ti 3d orbit.

here to calculate the electronic band structure and corresponding electronic density of states (EDOS). As shown in Fig. 1(b), there are two valleys in the valence band: V_1 at M (twofold degeneracy) and V_2 at R (fourfold degeneracy), and the energy difference between them is very small (around 10 meV) compared with $k_B T$, which could be regarded as effective band convergence. More interestingly, this degenerated electronic state is relatively flat at the VB edge, which has been verified to be beneficial for good Seebeck coefficients in complex band-structure materials [50,51]. Similarly, the conduction band exhibits two valleys: C_1 at midpoint of Γ-X and C_2 at X (twofold degeneracy), also showing a small energy difference. At relatively high temperature (thermal energy is sufficient), the valleys C_1 and C_2 become degenerate, and both contribute to improve the n-type Seebeck coefficient. Note that the degeneracy level of the valence band valleys is more than that of the conduction ones, indicating better TE performance under p-type doping. Meanwhile, the atomic orbital's projected band structure illustrates that the conduction band edge is mainly contributed by Ti d orbitals, while Cu d orbitals represent the main contribution to the valence band edge. Considering that the Cu $3d$ and Ti $3d$ states contain almost all the contributions to the edge of the band, the contribution of Se atoms is negligible (not shown for clarity), which is also applicable to other similar structures [52].

To understand the relationship between the vibration properties and the crystal structure, we calculate the phonon dispersion curves of Cu_4TiSe_4, as demonstrated in Figs. 2(a)–2(c). Apparently, there are no imaginary modes in the entire BZ, indicating that the system is dynamically stable at the ground state. To further evaluate the stability of Cu_4TiSe_4 at high temperatures, we also perform the *ab initio* molecular dynamics (AIMD) calculations via a 5000-step MD simulation in the temperature range of 400−700 K. The obtained results show the total potential energy fluctuates slightly and the geometric distortion is not obvious, confirming the thermodynamic stability of Cu_4TiSe_4 at high temperature. Since the unit cell of Cu_4TiSe_4 contains nine atoms, there are 27 phonon branches, which are composed of three acoustic phonon

branches [two transverse acoustic (TA and TA′) modes, one longitudinal acoustic (LA)] and 24 optical phonon branches. Here, the phonon dispersion could roughly be divided into three frequency regions: low (0–2.5 THz), medium (2.5–4.5 THz), and high (4.5–10 THz). According to the atom-resolved projected band structure in Fig. 2, the low-frequency phonon modes are mainly contributed by the vibration of heavier Cu and Se atoms with almost the same amplitude, whereas the medium-frequency phonon modes come mostly from the Cu atoms. The lighter Ti atoms only participate in a few high-frequency optical contributions, similar to the behavior of Cu_3VSe_4 [53]. Thus, proper doping at Cu and Se sites might be conducive to obtain low lattice thermal conductivity. Additionally, the low-frequency optical branches cross the acoustic branches, which increases the scattering rates of acoustic phonons and results in low thermal conductivity [21,54]. Another noteworthy feature of the dispersion curves is the existence of phonon gaps in the optical phonon branches [as marked in Fig. 2(c)]. Previous studies have verified that the presence of a phonon gap can forbid lots of three-phonon scattering processes that must satisfy the restriction of simultaneous energy and momentum conservation [55,56], also suggesting the four-phonon interaction is crucial to quantify the thermal conductivity of various solid crystals such as BAs [57] and AlSb [58]. In addition to the phonon gap, one can see that most medium- and high-frequency optical branches are very flat, and so the three-optical-phonon scattering processes will be substantially weakened because of the energy selective rule, as reported previously [59]. To sum up, the κ_l of Cu_4TiSe_4 might be relatively low after considering the four-phonon interaction.

B. Electron and phonon transport properties

Motivated by the prominent band convergence effect in Cu_4TiSe_4, we perform electron transport calculations to determine thermometric performance. Before evaluating the thermoelectric parameters, it is necessary to figure out the carrier relaxation time τ_e in terms of Eqs. (1)–(3). To obtain the rational τ_e, the effects of impurity, acoustic
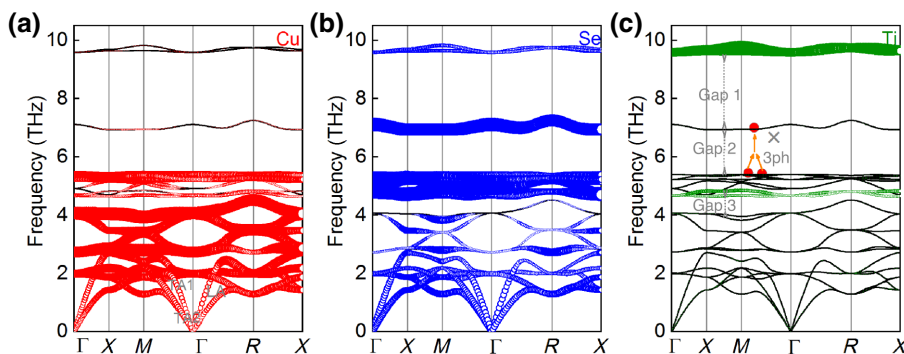

FIG. 2. Phonon dispersion of Cu_4TiSe_4 along the high-symmetry q points in the irreducible BZ. The relative contributions of (a) Cu, (b) Se, and (c) Ti atoms are represented by bubbles. The cross in Fig. 3(c) denotes that the large band gap will restrict three-phonon scattering in the high-frequency range.
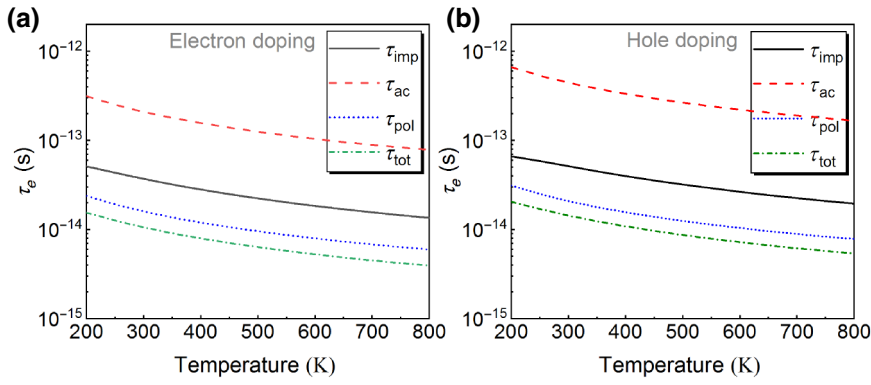
FIG. 3. Electron relaxation time under different scattering mechanisms for (a) n- and (b) p-type Cu$_4$TiSe$_4$ as a function of temperature T at the concentration of 5×10^{20} cm^{-3}.

phonon, and polar optical phonon scatterings on relaxation times are taken into account in the calculation. The obtained τ_e as a function of temperature (T) for both n-type and p-type structures is displayed in Fig. 3. Since the valence band near point M has a large dispersion, the small hole effective mass compresses the acoustic phonon scattering phase space, limiting the carrier scattering process [32]. Further confirmation of the contribution of polar phonon scattering can be made by comparing the scattering rate and the shape of the density of states based on the calculated complete electron-phonon scatterings (beyond the scope of the deformation potential theory), as reported in the literature [60–62]. In addition, as the temperature

increases, the carriers are more likely to be scattered, and τ_{op} is much smaller than τ_{ac} and τ_{imp}. Hence, the total relaxation time τ_e is determined by τ_{op}. The result is similar to the finding in GaN [42] and PbSe [9], but is quite different from that in GeSe [63].

After obtaining τ_e, the Seebeck coefficient S, thermoelectric power factor $S^2\sigma$, and electronic thermal conductivity κ_e are calculated and plotted in Fig. 4. Obviously, the thermoelectric parameters for electron and hole doping change with n in a similar way. Meanwhile, the electrical conductivity σ and Seebeck coefficient S present opposite trends with increasing n, thus leading to a maximum PF at $n = 10^{21}$ cm^{-3}. That is, the doping strategy is an effective

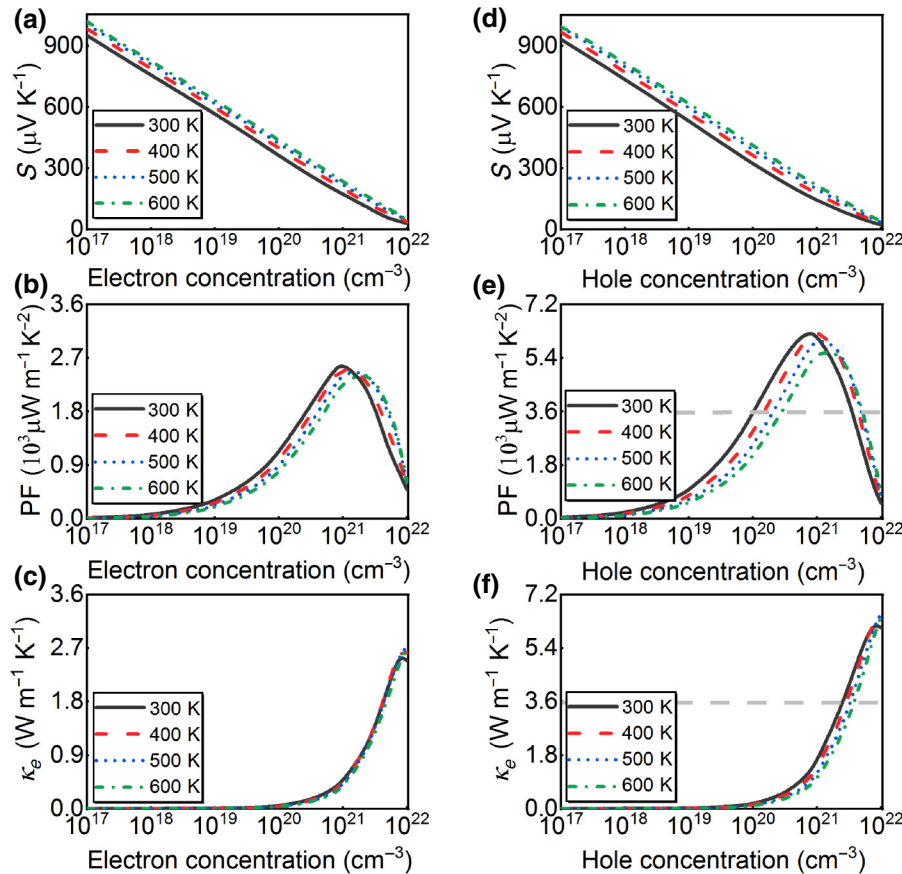FIG. 4. (a),(d) Seebeck coefficient S, (b),(e) power factor PF, and (c),(f) electronic thermal conductivity κ_e of n-type (left column) and p-type (right column) doping as a function of carrier concentration (ranging from 10^{17} to 10^{22} cm^{-3}) at different temperatures. Here, the dashed lines in (e),(f) denote the maximum range of power factor and electrical thermal conductivity for the n-type doping.

way to optimize TE performance. In addition, S increases slightly with increasing temperature T. Therefore, low n and T are beneficial to promote S. At 300 K, the value of S is close to 800 μV K^{-1} at $n = 10^{18}$ cm^{-3} for both n-type and p-type systems, which is larger than that of Mg$_3$Sb$_2$ [64] and Na$_2$AgSb [65], and effectively competes with K$_2$Se$_2$ with outstanding TE performance [32]. The large S could be attributed to the higher EDOS induced by the significant valence band degeneracy (cf. Fig. 1), where strong band asymmetry above and below the Fermi level enables the electron-hole compensation to be weakened. For PF, which describes how much electricity is generated, Figs. 4(b) and 4(e) show that the maximum value of PF achieves 6.0 mW m^{-1} K^{-2} near the carrier concentration of 8×10^{20} cm^{-3} in the p-type doped system, which is about 2 times higher than that for n-type doping. This is because σ has a greater influence on the PF than S, and the small hole effective mass that originates from the flatness of the valence band near the edge gives rise to higher σ. For the electronic thermal conductivity κ_e, it increases with n, and p-type doping is more efficient in boosting κ_e than the n-type counterpart, as expected. That can be explained by the Wiedemann-Franz law where κ_e is proportional to σ (see Appendix B for more details). Owing to the low κ_l of Cu$_4$TiSe$_4$, κ_e gives an important contribution to the total κ, particularly in the range of $n > 5 \times 10^{20}$ cm^{-3}. Hence, choosing an appropriate concentration to counteract the adverse effect of κ_e is conductive to obtain optimal TE performance.

Typically, the lattice thermal conductivity κ_l is a critical factor for high TE conversion efficiency since κ_l exceeds κ_e for most semiconductors. Hence, we calculate the temperature-dependent κ_l of Cu$_4$TiSe$_4$. Here, the three-phonon and four-phonon processes are considered in the computation. As shown in Fig. 5(a), κ_l presents obvious isotropy owing to the unique atomic arrangement of the $P43m$ group (high degeneracy symmetry). Meanwhile, κ_l gradually decreases with the increase of temperature, revealing a behavior typical of crystalline materials. At 300 K, the calculated κ value considering only three-phonon scattering is 3.6 W m^{-1} K^{-1}, which is higher than other promising TE materials such as GaSe$_{0.5}$Te$_{0.5}$ alloy [49] and Sr$_3$AlSb$_3$ [66] under the same calculation conditions. The relatively low κ_l could be attributed to heavy atomic masses and the crossover between acoustic and low-frequency optical branches. Moreover, it is found that the Cu$_4$TiSe$_4$ compounds lie in the region of the defined metavalent bond, indicating strong lattice anharmonicity because of the large charge transfer (see Appendix C for qualitative analyses). To distinguish the contribution of phonons in different frequency ranges, the cumulative κ_l of Cu$_4$TiSe$_4$ in the temperature range 300–600 K versus the phonon frequency is plotted in Fig. 5(b). As expected, the acoustic phonons with frequencies below 2 THz contribute 90% of the κ_l, and optical phonons contribute less to heat conduction. Actually, the major role of optical phonons is here to provide various three-phonon scattering channels for the heat-carrying acoustic phonons. Moreover, it is clear that the cumulative values from acoustic phonons consistently deviate from each other at different temperatures, suggesting the inverse temperature effect on the vibrational properties has
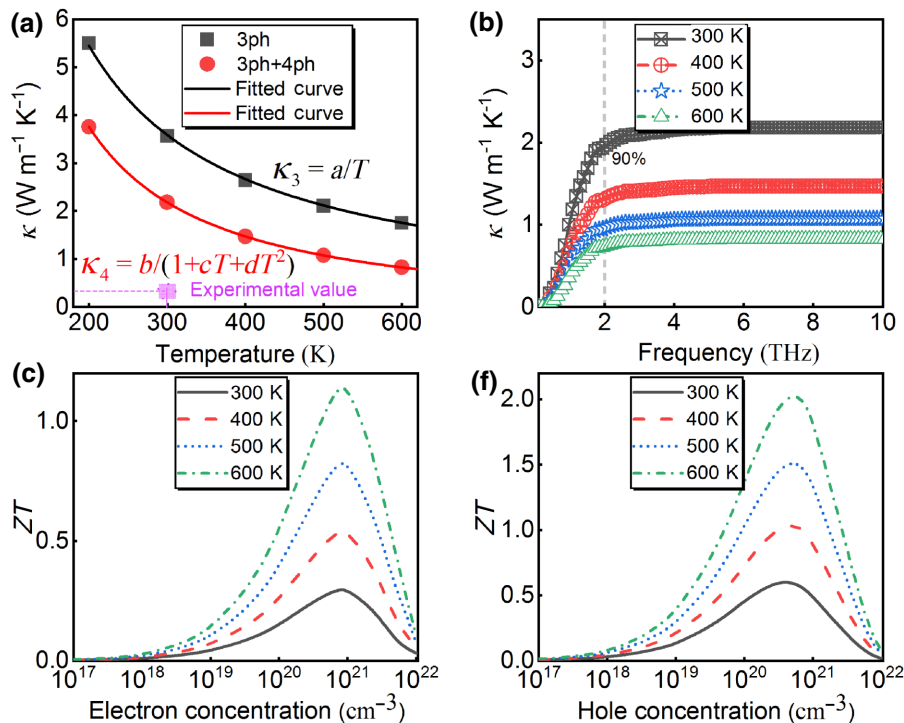

FIG. 5. (a) κ_l as a function of temperature for Cu$_4$TiSe$_4$. Here, the black and red lines represent the fitted curves using $\kappa_l \sim T^{-1}$ and $\kappa_l \sim (AT + BT^2)^{-1}$ for the cases without and with the four-phonon term in the computation process, respectively. (b) Frequency-dependence of cumulative κ_l at 300 K. Calculated ZT value of (c) n-type and (d) p-type doped Cu$_4$TiSe$_4$ versus carrier concentration at 300–600 K.

been captured from the microscopic aspect. After including four-phonon scattering, the obtained κ_l differs clearly from that considering only three-phonon scattering. At 300 K, the κ_l decreases from 3.6 to 2.2 W m^{-1} K^{-1}, corresponding to an almost 39% reduction. It can be understood that the existence of the phonon gap and the flattening of the optical branches forbid considerably more phonon scattering channels for the three-phonon process than the four-phonon process. Previous studies have also reported that the κ_l of BAs and AlSb are separately decreased by 37% and 50% at 300 K after including four-phonon scattering [66]. Furthermore, as temperature increases to 800 K, the reduction of κ_l can reach 60%. In brief, four-phonon scattering plays a significant role in determining the κ_l value, especially at relatively high temperatures. Another interesting observation in Fig. 5(a) is that the temperature dependence of κ_l follows a typical T^{-1} law when three-phonon scattering is considered, consistent with common knowledge in solid-state physics. After considering four-phonon scattering, the decreasing trend of κ_l follows the relationship $\kappa_l \sim (AT + BT^2)^{-1}$, which agrees well with the previous findings [56].

In order to explore the underlying mechanism responsible for the low κ_l of Cu$_4$TiSe$_4$, the mode-resolved (LA, TA1, TA2) and all acoustic mode (AA) contributions to κ_l are displayed in Fig. 6. Obviously, the acoustic modes make dominant contributions to the κ_l in contrast to the optical modes, further validating the observations in Fig. 4(b). When only three-phonon scattering is considered, the TA1 and TA2 branches have an almost equal contribution (35%) to the total κ_l, while the percentage contribution of the LA branch is relatively small (22%) at 300 K because the crossover between LA and low-frequency optical branches leads to strong internal scattering [67]. After including four-phonon scattering, additional phonon scattering channels that involve acoustic phonons are opened. Hence, the contribution of LA and TA1 branches are reduced from 22% to 19% and from 35% to 30% at 300 K, respectively. By contrast, the TA2 contribution increases from 35% to 38%, similar to what was found in AlSb [59]. This behavior can be

explained in that there is no significant crossover between the TA2 and other phonon branches [Fig. 2(a)], suggesting weak scattering of the TA2 branch. Meanwhile, the contribution of all optical modes increases to some extent. In brief, the four-phonon effect is not only associated with the crossover between acoustic and optical branches, but also the bunching of optical branches, which suppresses the phase space for the three-optical-phonon scattering channels but hardly affects the three-optical-phonon scattering [59]. For a clearer insight into the low κ_l, the mode-level analyses of phonon scattering rates and group velocities are conducted. Figure 6(b) demonstrates the frequency dependence of phonon scattering rates including isotope-, three-, and four-phonon scattering events at 300 K. At first glance, the phonon scattering rates due to different mechanisms all increase with the frequency, and span several orders of magnitude (10^{-4}–10^1 ps^{-1}) in the whole frequency range. Moreover, compared to anharmonic phonon-phonon scattering, the isotope scattering is negligibly weak for acoustic phonons, while that for high-frequency optical modes is comparable to the three- and four-phonon scattering, suggesting the isotope effect becomes less important to thermal transport at higher temperature. Interestingly, the four-phonon scattering rates are slightly smaller than those of the three-phonon counterparts in the low-frequency range (<2 THz), highlighting the important role played by the four-phonon process. With a further increase of temperature, the four-phonon scattering rates become practically overlapped with and even become larger than the three-phonon counterparts (not shown for simplicity). Actually, phonon group velocity V_g is another factor in the low κ_l, as formulated in Eq. (3) [68,69]. As shown in Fig. 6(c). it can be seen that V_g is close to zero for most of the optical modes, while the acoustic modes possess relatively large V_g. Concretely, the V_g values of LA, TA1, and TA2 branches along the Γ-M high-symmetry solution are 4.3, 3.7, and 3.4 Km s^{-1} in the long-wavelength limit, respectively, which are far lower than those in high-thermal-conductivity materials [70,71], but are of the same order of magnitude as Tl$_3$VSe$_4$ [72] and K$_2$Se$_2$ crystals [32] with ultralow κ_l. When the frequency
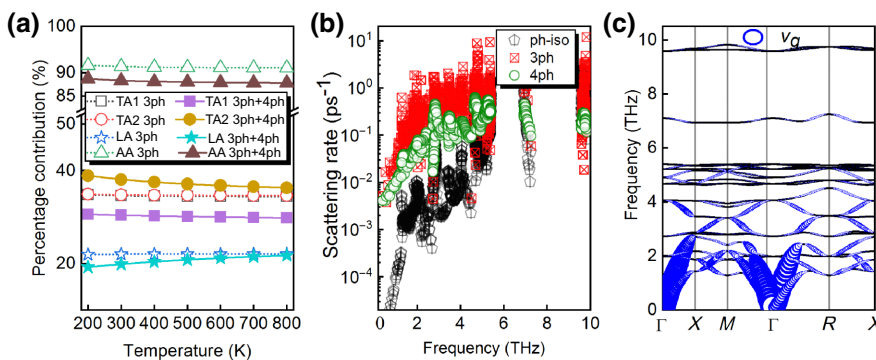

FIG. 6. (a) Percentage contribution of each phonon branch to thermal conductivity as a function of temperature for Cu$_4$TiSe$_4$. Here, both three-phonon and four-phonon scatterings are considered. (b) Phonon scattering rates due to isotope-, three-, and four-phonon scattering events at 300 K. (c) Phonon dispersion along the high-symmetry q points and the group velocity values represented by bubbles.

exceeds 2 THz, the V_g values of most of the acoustic modes also tend to be zero. Therefore, we can attribute the low κ_l of Cu_4TiSe_4 to the low phonon group velocity and the large four-phonon scattering rates existing in the low-frequency range.

C. TE properties

After all the thermoelectric coefficients are obtained, we can calculate the ZT value versus the temperature and carrier concentration for the two doping types. As show in Figs. 5(c) and 5(d), the ZT value of the n-type-doped system first increases to a peak value of 0.3 at the optimal n of 8×10^{20} cm^{-3} at 300 K, followed by a rapid decrease to small values. As temperature increases, the maximum ZT also gradually increases. Moreover, the maximum ZT value of the p-type doped system is superior to that of the n-type counterpart, which could be attributed to the difference between VBM and CMB bands. At 500 K, the maximum ZT values for two doping types are 0.82 and 1.49, respectively. Although the optimal ZT value of p-doped Cu_4TiSe_4 is lower than 3 at medium temperatures (around 500 K), it still surpasses some promising TE materials such as GeSe [63] and LaMOCh [73]. What is notable is that the optimal n for the maximum ZT moves to the low-concentration region compared with the maximum PF, and the difference between the two cases is attributed to the fact that κ_e becomes increasingly important at this concentration range [26]. For this, the subsequent calculation of TE properties is primarily focused on the p-type doped system.

D. Effect of strain on thermoelectric parameters

Strain engineering has proved to be an effective and feasible tool for tuning thermal [74,75] and electronic [76,77] properties. Additionally, it could be used to enhance TE performance through band convergence [49,78] and phonon softening [9,79] effects. Here, 1.5% and 2.25% isotropic tensile strains [$\varepsilon = (l - l_0)/l_0$] are applied to Cu_4TiSe_4 as representative cases. Figure 7(a) shows the triaxial tensile-strain-dependent PF at 500 K. Clearly, the PF decreases significantly with ε at given carrier concentration. For the unstrained case, the maximum PF value reaches 5.9 mW m^{-1} K^{-2} near the carrier concentration of 10^{21} cm^{-3}, while under $\varepsilon = 2.25\%$, PF shows a large reduction of 64% compared with the unstrained case. The remarkable reduction of PF stems from the insensitivity of S and the great decrease of σ with increasing ε, where the former depends on the shape of the band structure that is only weakly affected by tensile strain [50], whereas the latter is ascribed to the large enhancement of electro-optical phonon scattering rates. It is well known that σ is directly proportional to κ_e according to the Wiedemann-Franz law as $\kappa_e = L\sigma T$. As shown in Fig. 7(b), κ_e depends on ε more and more at higher carrier concentration, and becomes less sensitive at lower carrier concentration. At 8×10^{20} cm^{-3} carrier concentration, κ_e is 0.87 W m^{-1} K^{-1} and κ_l is 1.05 W m^{-1} K^{-1} at 500 K for the unstrained case. In comparison, a 2.25% tensile strain leads to a reduction in κ_e and κ_l by almost 45% and 75%, respectively. That is, κ_e and κ_l are comparable to each other under large strain and carrier concentration. Although the
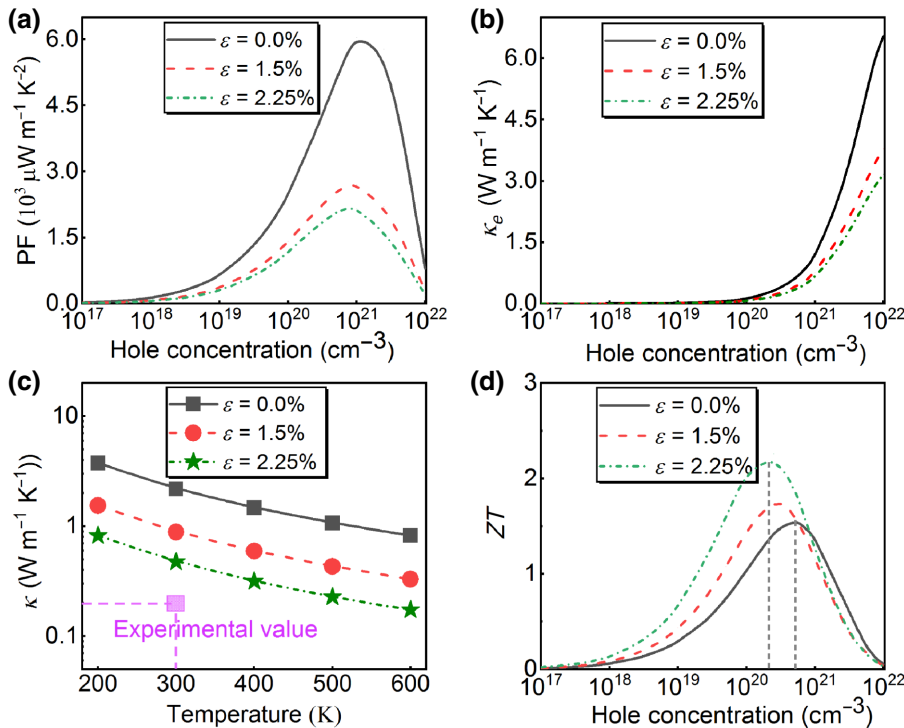

FIG. 7. (a) Power factor PF, (b) electronic thermal conductivity, (c) lattice thermal conductivity, and (d) ZT value of p-type Cu_4TiSe_4 as a function of carrier concentration under different tensile strains.

remarkable decrease in PF might seem unfavorable to improving TE performance, the final ZT value is a result of the complicated change of the PF and thermal conductivity ($\kappa_e + \kappa_l$). On the other hand, the strain-dependent κ_l as a function of temperature is shown in Fig. 7(c). Clearly, κ_l decreases significantly with the increase of ε. This is because the applied tensile strain lengthens the bond length, weakens the interatomic forces, and causes phonon softening (low group velocity) [79]. At 300 K, the calculated κ_l is 2.2 W m^{-1} K^{-1} under $\varepsilon = 0\%$, which is higher than the experimental result (about 0.2 W m^{-1} K^{-1}) [36]. This overestimation can be understood as the existence of structural defects such as impurity, vacancy, grain boundary, and residual strain in the experimental samples give rise to additional phonon scattering that plays a more important role compared with the intrinsic phonon scattering. When $\varepsilon = 2.25\%$, the value of κ_l is reduced by about 77% (0.48 W m^{-1} K^{-1}). A similar significant reduction trend in κ_l caused by isotropic strain has been reported in previous studies [80,81]. In fact, the strong dependence of κ_l on tensile strain can be partially explained by the remarkably enhanced four-phonon scattering rates, as discussed in detail in the following.

By combining the electron and phonon transport parameters, we obtain the corresponding ZT value under different ε and plot it in Fig. 7(d). From this graph, it can be seen that the applied triaxial strain results in a marked increase in ZT value compared with that in the unstrained system. This is because there is relatively low PF and ultralow thermal conductivity. To be specific, the maximum ZT of p-type Cu$_4$TiSe$_4$ increases slightly at $\varepsilon = 1.5\%$ because of the significant decrease of PF [see Fig. 7(a)], but increases significantly at $\varepsilon = 2.25\%$ due to the significant reduction in κ_l. In the case of $\varepsilon = 2.25\%$, the maximum ZT achieves 2.2 with a p-doping concentration of about 2×10^{20} cm^{-3} at 500 K, which is comparable to bulk TE materials, such as Sr$_2$BiAu [26] and K$_2$Se$_2$ [63], and indicates promising application in medium-temperature TE devices. It is worth noting that the optimal n for the maximum ZT is significantly reduced when ε increases from 0% to 2.25%. This can be explained in that the strong suppression of phonon heat transport caused by triaxial tensile strain allows the optimal n to be reduced and ZT tends

to peak at both a small κ_e and a large Seebeck coefficient [82]. The reoptimized carrier concentration would be helpful to prepare experimentally the Cu$_4$TiSe$_4$-based TE devices [83].

In order to interpret the reasons for the tensile-strain-dependent thermal conductivity of Cu$_4$TiSe$_4$, we calculate the averaged total Gruneisen parameter $\left(\bar{\gamma} = \sqrt{\sum ((V/\omega)(\partial\omega/\partial V))^2}\right)$ with respect to ε, which can qualitatively characterize the anharmonic degree of crystal structure. At 500 K, the $\bar{\gamma}$ values under $\varepsilon = 0\%$, $\varepsilon = 1.5\%$, and $\varepsilon = 2.25\%$ correspond to 1.5, 1.8, and 2.0, respectively, indicating the strong anharmonicity of Cu$_4$TiSe$_4$ under high strain. The modulated lattice anharmonicity is comparable to that of the well-known SnSe [84] and Ba$_3$AlSb$_3$ [66] compounds with strong anharmonicity. Meanwhile, the mode-resolved phonon scattering rates due to three- and four-phonon scattering events with respect to ε at 500 K are plotted in Fig. 8. Because the phonon-isotope scattering indicates a negligible contribution to heat conduction [see Fig. 6(b)], it is not presented for simplicity and the blue points indicate the scattering rate equals twice the phonon frequency according to the previous studies [85–87]. Additionally, the four-phonon scattering rates compare well with those of the three-phonon counterparts in the frequency range of $0-2$ THz (corresponding to the acoustic phonons). In this case, the role of four-phonon scattering becomes more important than at 300 K [see Fig. 6(b)]. In Fig. 8, the phonon spectra shift towards low frequency (redshift) in triaxially strained structures where the interatomic interactions are softened, as expected. As a consequence of the redshift, phonon branches become denser. Furthermore, both the three- and four-phonon scattering rates have an obvious enhancement under $\varepsilon = 1.5\%$. Specifically, the four-phonon scattering rates are largely overlapped with the three-phonon counterparts, suggesting that four-phonon scattering is a characteristic feature of the strain-driven anharmonic lattices and should be rigorously taken into account in calculations. As ε increases to 2.25%, the intrinsic phonon scattering rates become large, and the four-phonon scattering rates are comparable to the three-phonon scattering counterparts in the acoustic-phonon frequency range. In fact,
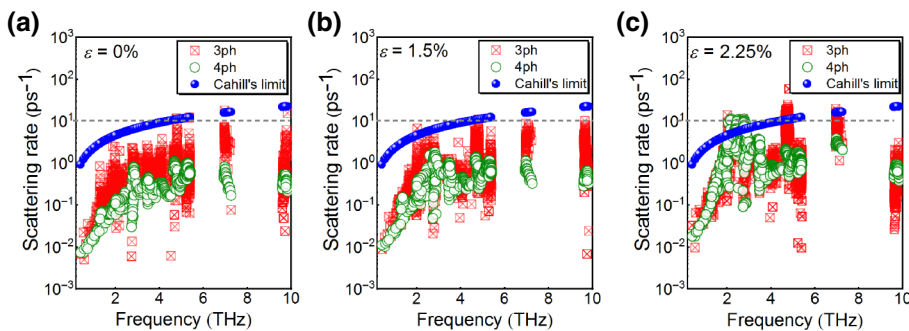

FIG. 8. Phonon scattering rates due to three- and four-phonon scattering events at 500 K for (a) $\varepsilon = 0\%$, (b) $\varepsilon = 1.5\%$, (c) $\varepsilon = 2.25\%$. Here, the horizontal dashed lines represent a reference corresponding to the maximum values of phonon scattering rates in the strain-free structure.
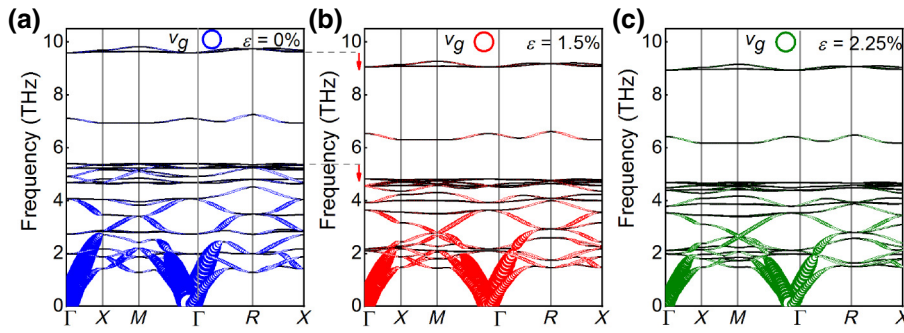
FIG. 9. Phonon dispersion along the high-symmetry q points in the irreducible BZ with the group velocity values represented by bubbles for (a) $\varepsilon = 0\%$, (b) $\varepsilon = 1.5\%$, and (c) $\varepsilon = 2.25\%$.

the phenomenon could be understood from the analysis of the dispersion relation, where the lowest-lying optical (LLO) branches present avoided crossings with the LA phonons, manifesting the coupling between the LLO and LA branches. The detailed discussion about the role of the avoided crossings of phonon dispersions in reducing lattice thermal conductivity under different strains can be found in Appendix D. When $\varepsilon \geq 3\%$, the validity of the particle-like phonon picture is discussed in Appendix E. Considering that the acoustic phonons can dominate lattice thermal conductivity in Cu_4TiSe_4, the remarkably enhanced four-phonon scattering rates caused by triaxial tensile strain are believed to be responsible for the significant reduction in κ_l. Phonon group velocity v_g is another important factor influencing κ_l. As shown in Fig. 9, it can be seen that as the interatomic bond length undergoes axial elongation (softening) upon applying strain, the phonon spectra exhibit an obvious redshift (denoted by the red arrows). Moreover, the influence of tensile strain on the chemical bonding characteristics of Cu_4TiSe_4 are studied in Appendix C. The emergence of the redshift phenomenon gives rise to the following two factors: First, both group velocity and specific heat are reduced to some extent, as reported in previous studies [22]. On the other hand, as the redshift amplitude increases gradually with ε, the energy gap between different phonons becomes small, and thus the overall probability of the intrinsic phonon-phonon scattering increases. More importantly, the optical phonons could hybridize with acoustic modes in the low-frequency range, where the recombination processes of four-phonon scattering more easily occur, supporting the preceding analysis in Fig. 8. In short, the primary reason for the significant reduction in κ_l with respect to ε should be the phonon scattering rates rather than group velocity.

IV. CONCLUSION

In conclusion, inspired by experimentally reported inherent advantages, the TE properties of Cu_4TiSe_4, in which the liquid-like movement of Cu+ cations allows a low thermal conductivity to be reached, are theoretically studied via combining the BTE and first-principles calculations. Our main finding is that the four-phonon scattering significantly influences the lattice thermal conductivity of Cu_4TiSe_4 even at room temperature. On the other hand, the coexistence of high dispersion and valley degeneracy at the top valence band in the electronic structure causes a high power factor. Consequently, the isotropic ZT value of 1.5 at 500 K is captured in the p-type doped Cu_4TiSe_4. In addition, the value of ZT can be further enhanced to 2.2 by applying 2.25% tensile strain, which is ascribed to the remarkably enhanced four-phonon scattering processes induced by the tensile strain. Our work highlights the promising possibility of Cu_4TiSe_4 and similar systems for high-performance TE applications at medium temperature.

APPENDIX A: THE CONVERGENCE TEST FOR LATTICE THERMAL CONDUCTIVITY

Here, a q-point grid of $14 \times 14 \times 14$ is used to map the reciprocal space of phonons for calculating the lattice thermal conductivity after conducting a test of up to a $18 \times 18 \times 18$ q-point grid where the difference in thermal conductivity is 0.043 W m^{-1} K^{-1} higher for a $16 \times 16 \times 16$ q-point grid and 0.082 W m^{-1} K^{-1} higher for a $14 \times 14 \times 14$ q-point grid, as shown in Fig. 10. The relative difference is within 5%, indicating a satisfactorily converged value of lattice thermal conductivity. Because four-phonon scattering calculations are very expensive at a larger broadening factor, we set scalebroad = 0.1 where the available four-phonon processes are already around 10^{10} in calculations at all temperature points, as suggested by previous research [24].
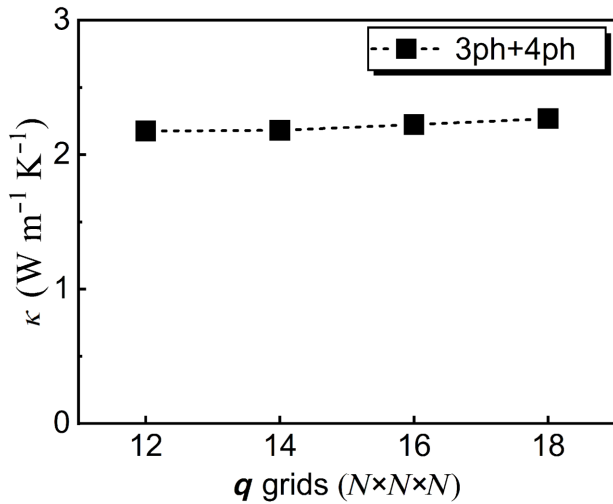
FIG. 10. Convergence test for the lattice thermal conductivity of Cu_4TiSe_4 with respect of the q-point mesh. The value of scalebroad is taken as 0.1.

APPENDIX B: THE RELATIONSHIP BETWEEN ELECTRICAL CONDUCTIVITY AND ELECTRONIC THERMAL CONDUCTIVITY

Here, the electrical thermal conductivity κ_e is insensitive to temperature as compared to the Seebeck coefficient S in Fig. 4. In contrast, the electronic conductivity σ is sensitive to temperature. To be specific, the electrical conductivity decreases with increasing temperature, as shown Fig. 11. For instance, at a low (high) carrier concentration of 1×10^{19} cm^{-3} (5×10^{21} cm^{-3}), the values of σ in p-type doped Cu_4TiSe_4 are 3449.8 S m^{-1} (876 001.2 S m^{-1}) and 1417.1 S m^{-1} (461 092.3 S m^{-1}) at 300 and

600 K, respectively. According to the Wiedemann-Franz law $\kappa_e = L\sigma T$, the increasing T can effectively offset the decrease of σ, and hence κ_e seems insensitive to T. Similar analysis results have been reported in previous studies [49,52,88].

APPENDIX C: THE CHEMICAL BONDING CHARACTERISTICS IN Cu_4TiSe_4 UNDER DIFFERENT TENSILE STRAINS

Metavalent bonding plays a vital role in lattice anharmonicity [89–91]. Therefore, the transferred and shared charges are calculated by the density-derived electrostatic and chemical (DDEC6) method as implemented in CHARGEMOL [92,93]. Concretely, the shared charge is presented as twice the DDEC6 overlap population, as it is a count of the electron pairs shared. The transferred charge is calculated directly from the DDEC6 net atomic charges on each atom. The obtained transferred charge in the selenides is around 0.861$|e|$ and the shared charges between Se and Cu atoms is 0.945 $|e|$. According to the two-dimensional map of shared and transferred charges in previous studies [88,94–96], the Cu_4TiSe_4 compounds studied herein lie in the region of the defined metavalent bond alongside other ternary chalcopyrites such as PbTe, which has strong anharmonicity due to the higher charge transfer [94]. As shown in Fig. 12, when tensile strain increases from 0% to 3%, the transferred charge greatly increases from 0.861$|e|$ to 1.235$|e|$, where the type of bonding of Cu_4TiSe_4 lies in the region of the defined ionic bond alongside BaSe and BaTe [94,95]. Hence, the significant increase of charge transfer bonding could promote the anharmonicity of the lattice vibrations.
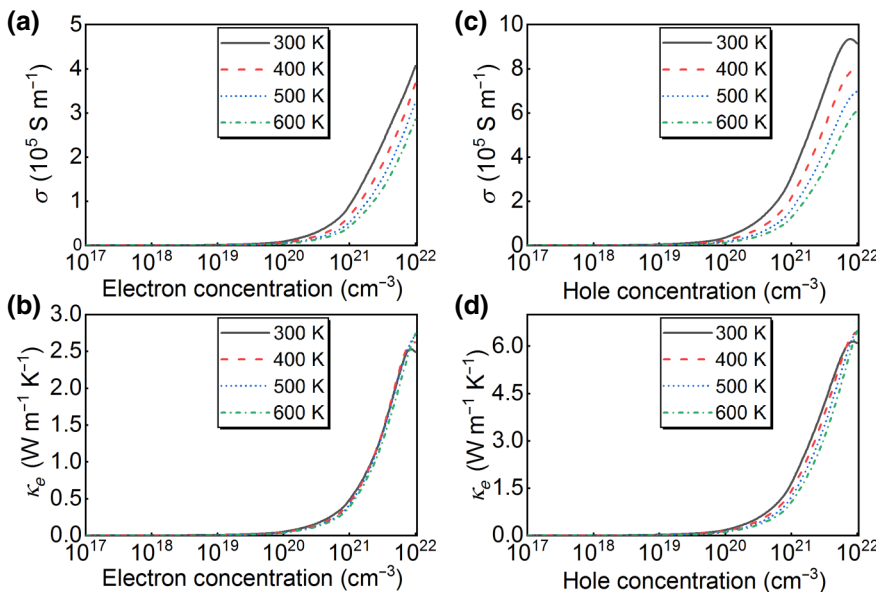

FIG. 11. (a),(c) Electrical conductivity, (b),(d) electronic thermal conductivity of n-type (left column), and p-type (right column) doping as a function of carrier concentration at different temperatures.
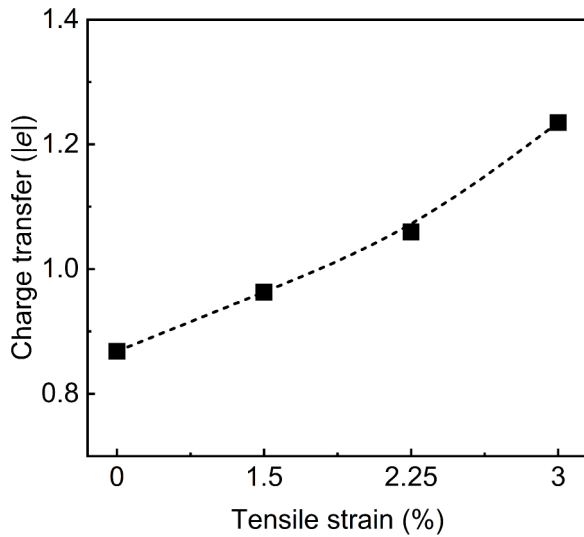
FIG. 12. Transferred charge in the Cu_4TiSe_4 as a function of tensile strain.

APPENDIX D: THE ROLE OF THE CROSSOVER POINTS OF PHONON DISPERSIONS IN PHONON TRANSPORT

The phonon dispersions along the highly symmetric G-X direction of the primitive cell under different tensile strains are plotted in Fig. 13 and the complete phonon dispersions can be found in Fig. 9. It is seen that there is significant crossover of the LA branch and the two lowest-lying optical (LLO1 and LLO2) branches in the strain-free case. Although these optical phonons do not directly contribute to the transformation of heat conduction because of the low group velocity, they can lead to the higher probability of scattering for the LA modes. As a result, the percentage contribution of the LA branch is relatively small [around 20% see Fig. 6(a)], even if the group velocity of this branch is large [see Fig. 6(c)]. When the loading strain increases to 2.25%, the dispersive LLO1 branch presents avoided crossings with the LA branch, manifesting the coupling between the LLO and LA branches. Moreover, in the vicinity of the avoided crossing point, a gap of about 0.3 THz is opened where the energies of the uncoupled basis states are equal. Here, the role of the LLO phonons in thermal transport becomes clear. On the one hand, the LLO branches suppress the LA branch by the avoided-crossing effect, as shown in Fig. 9, which causes the acoustic phonon group velocity to drop significantly to zero around 1.7 THz under 2.25% strain [16,97]. On the other hand, the strong coupling between the LA and LLO branches can greatly increase the scattering rates of LA phonons as shown in Fig. 8, reducing the portion of heat transferred by these acoustic phonons further [98–100]. As a result, the contribution of the LA branch to thermal conductivity significantly decreases with increasing tensile strain, as depicted in Fig. 14.
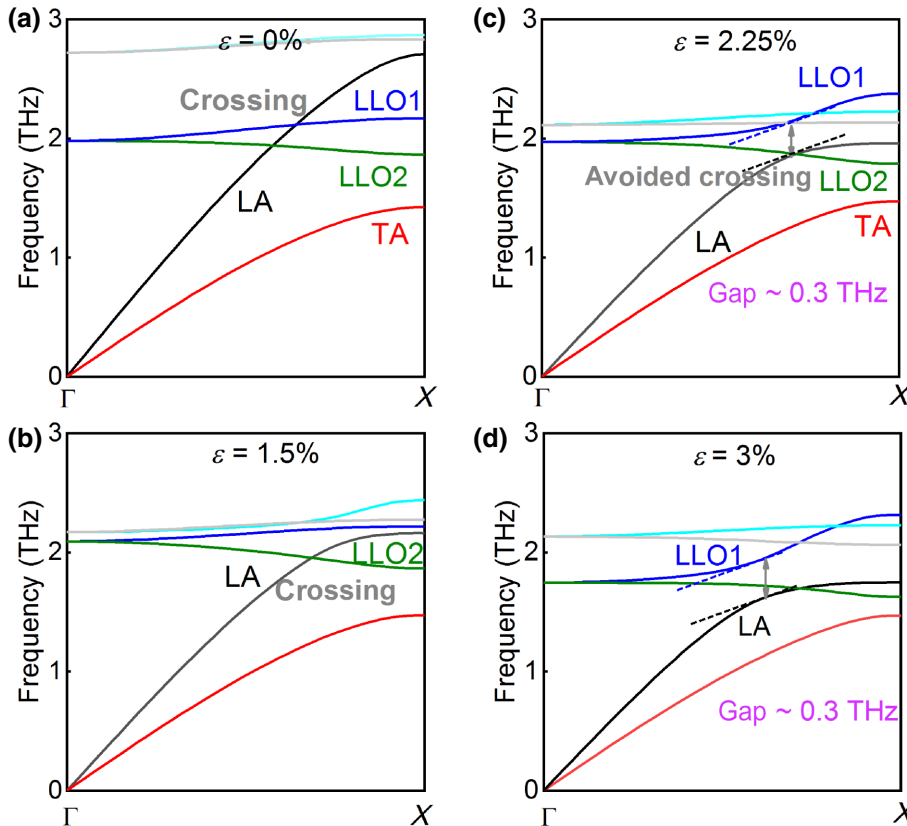

FIG. 13. Phonon dispersion along the high-symmetry q points in the irreducible BZ for (a) $\varepsilon = 0\%$, (b) $\varepsilon = 1.5\%$, (c) $\varepsilon = 2.25\%$, and (d) $\varepsilon = 3\%$. The crossing and avoided crossing between the lowest optical phonon branch and the LA branch is remarkable in (a),(b) and (c),(d), respectively.
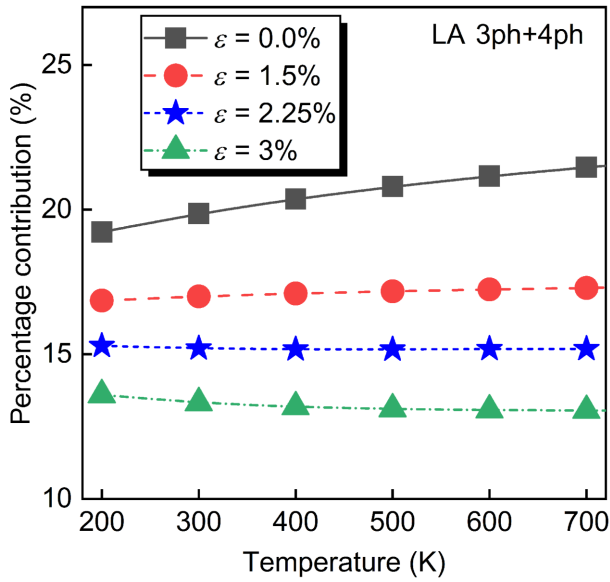
FIG. 14. Contribution of the LA branch to lattice thermal conductivity as a function of temperature under different tensile strains.

FIG. 15. Phonon scattering rates due to three- and four-phonon scattering events at 500 K for $\varepsilon = 3\%$.

APPENDIX E: THE VALIDITY OF THE PARTICLE-LIKE PHONON PICTURE IN STRAINED Cu_4TiSe_4

Normally, the phonon transport phenomena in crystals can be described by the Peierls-Boltzmann transport equation (PBTE) using a well-defined phonon quasiparticle picture. However, the PBTE was recently found to be insufficient for describing phonon transport in strongly anharmonic crystalline materials, such as Tl_3VSe_4 [72] and $CsPbBr_3$ [86], where the scattering rates of phonons are larger than the frequency of the phonons themselves. To check the suitability of the phonon quasiparticle picture in Cu_4TiSe_4, the curve with scattering rates that are twice the phonon frequency corresponding to the amorphous limit as proposed by Cahill *et al.* [85] is plotted in Fig. 8, and the phonon quasiparticle picture becomes valid when the data points are well below the reference line. From this graph, it can be seen that all strain-free three- and four-phonon scatterings are distributed below the reference line, supporting the validity of the BTE solutions. A similar analysis process has been reported in previous studies [72,87,101].

When the tensile strain is less than or equal to 2.25%, it can be seen in Fig. 8 that the vast majority of three- and four-phonon scatterings are distributed below the reference line, basically supporting the validity of the BTE solutions. When ε is larger than or equal to 3%, the three- and four-phonon scattering rates increase significantly and those of the phonons with frequencies between 1.2 and 4.0 THz are distributed above the reference line, leading
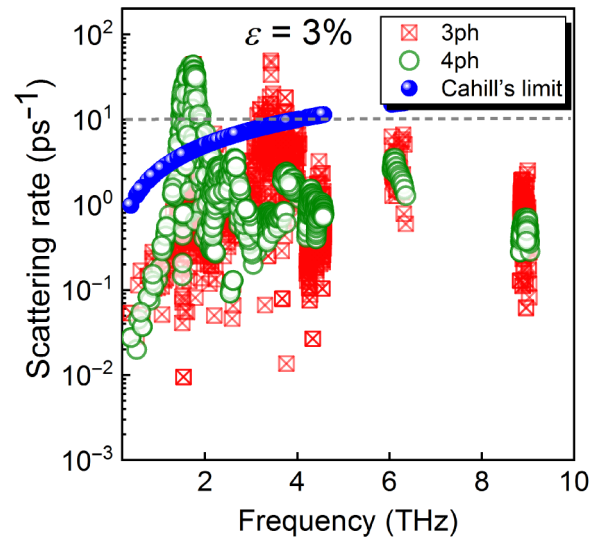
to a partial breakdown of the phonon quasiparticle picture, as shown in Fig. 15. Although the phonons with frequencies below 2 THz, which contribute about 85% of lattice thermal conductivity, are below the reference line, one cannot ignore the role of high-frequency phonons in contributing additional scattering channels to the low-frequency phonons. Hence, the results on high-strain cases (3%) are not discussed in detail. To overcome the shortcomings of ill-defined phonons induced by high strain, the temperature-dependent effective potential method based on the AIMD simulation can consider harmonic and anharmonic terms nonperturbatively [102]. On the other hand, self-consistent phonon theory combined with compressive sensing lattice dynamics is a recently proposed approach to include anharmonic effects, where the anharmonic frequency is estimated from the pole of the Green's function and the cubic and quartic IFCs are extracted by the compressive sensing techniques [103,104], which will be considered in our future work.

[1] J. P. Heremans, V. Jovovic, E. S. Toberer, A. Saramat, K. Kurosaki, A. Charoenphakdee, S. Yamanaka, and G. J. Snyder, Enhancement of thermoelectric efficiency in PbTe by distortion of the electronic density of states, Science **321**, 554 (2008).

[2] L. Yang, Z. G. Chen, M. S. Dargusch, and J. Zou, High performance thermoelectric materials: Progress and their applications, Adv. Energy Mater. **8**, 1701797 (2018).

[3] C. Fu, T. Zhu, Y. Pei, H. Xie, H. Wang, G. J. Snyder, Y. Liu, Y. Liu, and X. Zhao, High band degeneracy contributes to high thermoelectric performance in p-type half-Heusler compounds, Adv. Energy Mater. **4**, 1400600 (2014).

[4] W. Liu, X. Tan, K. Yin, H. Liu, X. Tang, J. Shi, Q. Zhang, and C. Uher, Convergence of Conduction Bands as a Means of Enhancing Thermoelectric Performance of *n*-Type $Mg_2Si_{1-x}Sn_x$ Solid Solutions, Phys. Rev. Lett. **108,** 166601 (2012).

[5] Y. Zhou and L. D. Zhao, Promising thermoelectric bulk materials with 2D structures, Adv. Mater. **29,** 1702676 (2017).

[6] T. Markussen, A. P. Jauho, and M. Brandbyge, Surface-Decorated Silicon Nanowires: A Route to High-*ZT* Thermoelectrics, Phys. Rev. Lett. **103,** 055502 (2009).

[7] D. Wu, L. Huang, P. Z. Jia, X. H. Cao, Z. Q. Fan, W. X. Zhou, and K. Q. Chen, Tunable spin electronic and thermoelectric properties in twisted triangulene π-dimer junctions, Appl. Phys. Lett. **119,** 063503 (2021).

[8] J. P. Heremans, M. S. Dresselhaus, L. E. Bell, and D. T. Morelli, When thermoelectrics reached the nanoscale, Nat. Nanotechnol. **8,** 471 (2013).

[9] P. Z. Jia, Z. X. Xie, Y. X. Deng, Y. Zhang, L. M. Tang, W. X. Zhou, and K. Q. Chen, High thermoelectric performance induced by strong anharmonic effects in monolayer $(PbX)_2(X = S, Se, Te)$, Appl. Phys. Lett. **121,** 043901 (2022).

[10] Y. J. Zeng, D. Wu, X. H. Cao, W. X. Zhou, L. M. Tang, and K. Q. Chen, Nanoscale organic thermoelectric materials: Measurement, theoretical models, and optimization strategies, Adv. Funct. Mater. **30,** 1903873 (2020).

[11] S. Lee, K. Esfarjani, T. Luo, J. Zhou, Z. Tian, and G. Chen, Resonant bonding leads to low lattice thermal conductivity, Nat. Commun. **5,** 3525 (2014).

[12] P. Acharyya, T. Ghosh, K. Pal, K. Kundu, K. Singh Rana, J. Pandey, A. Soni, U. V. Waghmare, and K. Biswas, Intrinsically ultralow thermal conductivity in Ruddlesden–Popper 2D perovskite $Cs_2PbI_2Cl_2$: Localized anharmonic vibrations and dynamic octahedral distortions, J. Am. Chem. Soc. **142,** 15595 (2020).

[13] M. Dutta, M. Samanta, T. Ghosh, D. J. Voneshen, and K. Biswas, Evidence of highly anharmonic soft lattice vibrations in a Zintl rattler, Angew. Chem., Int. Ed. **60,** 4259 (2021).

[14] T. Takabatake, K. Suekuni, T. Nakayama, and E. Kaneshita, Phonon-glass electron-crystal thermoelectric clathrates: Experiments and theory, Rev. Mod. Phys. **86,** 669 (2014).

[15] J. Li, W. Hu, and J. Yang, High-throughput screening of rattling-induced ultralow lattice thermal conductivity in semiconductors, J. Am. Chem. Soc. **144,** 4448 (2022).

[16] S. Xiong, K. Sääskilahti, Y. A. Kosevich, H. Han, D. Donadio, and S. Volz, Blocking Phonon Transport by Structural Resonances in Alloy-Based Nanophononic Metamaterials Leads to Ultralow Thermal Cconductivity, Phys. Rev. Lett. **117,** 025503 (2016).

[17] Z. Zhang, S. Hu, T. Nakayama, J. Chen, and B. Li, Reducing lattice thermal conductivity in schwarzites via engineering the hybridized phonon modes, Carbon **139,** 289 (2018).

[18] X. K. Chen, Z. X. Xie, W. X. Zhou, L. M. Tang, and K. Q. Chen, Phonon wave interference in graphene and boron nitride superlattice, Appl. Phys. Lett. **109,** 023101 (2016).

[19] S. I. Kim, K. H. Lee, H. A. Mun, H. S. Kim, S. W. Hwang, J. W. Roh, D. J. Yang, W. H. Shin, X. S. Li, Y. H. Lee, G. J. Snyder, and S. W. Kim, Dense dislocation arrays embedded in grain boundaries for high-performance bulk thermoelectrics, Science **348,** 109 (2015).

[20] S. Chen, Q. Wu, C. Mishra, J. Kang, H. Zhang, K. Cho, W. Cai, A. A. Balandin, and R. S. Ruoff, Thermal conductivity of isotopically modified graphene, Nat. Mater. **11,** 203 (2012).

[21] Z. X. Xie, X. K. Chen, X. Yu, Y. X. Deng, Y. Zhang, W. X. Zhou, and P. Z. Jia, Intrinsic thermoelectric properties in biphenylene nanoribbons and effect of lattice defects, Comput. Mater. Sci. **220,** 112041 (2023).

[22] C. W. Wu, X. Ren, G. Xie, W. X. Zhou, G. Zhang, and K. Q. Chen, Enhanced High-Temperature Thermoelectric Performance by Strain Engineering in BiOCl, Phys. Rev. Appl. **18,** 014053 (2022).

[23] Y. Pei, N. A. Heinz, A. LaLonde, and G. J. Snyder, High thermoelectric figure of merit in heavy hole dominated PbTe, Energy Environ. Sci. **4,** 2085 (2011).

[24] G. J. Tan, F. Y. Shi, S. Q. Hao, L. D. Zhao, H. Chi, X. M. Zhang, C. Uher, C. Wolverton, V. P. Dravid, and M. G. Kanatzidis, Non-equilibrium processing leads to record high thermoelectric figure of merit in PbTe–SrTe, Nat. Commun. **7,** 12167 (2016).

[25] L. D. Zhao, S. H. Lo, Y. Zhang, H. Sun, G. Tan, C. Uher, C. Wolverton, V. P. David, and M. G. Kanatzidis, Ultralow thermal conductivity and high thermoelectric figure of merit in SnSe crystals, Nature **508,** 373 (2014).

[26] J. Park, Y. Xia, A. M. Ganose, A. Jain, and V. Ozoliņš, High Thermoelectric Performance and Defect Energetics of Multipocketed Full Heusler Compounds, Phys. Rev. Appl. **14,** 024064 (2020).

[27] X. Tang, D. Fan, K. Peng, D. Yang, L. Guo, X. Lu, J. Dai, G. Wang, H. Liu, and X. Zhou, Dopant induced impurity bands and carrier concentration control for thermoelectric enhancement in p-type $Cr_2Ge_2Te_6$, Chem. Mater. **29,** 7401 (2017).

[28] T. Zhao, Y. Sun, Z. Shuai, and D. Wang, $GeAs_2$: A IV–V group two-dimensional semiconductor with ultralow thermal conductivity and high thermoelectric efficiency, Chem. Mater. **29,** 6261 (2017).

[29] J. F. Dong, F. H. Sun, H. C. Tang, J. Pei, H. L. Zhuang, H. H. Hu, B. P. Zhang, Y. Pan, and J. F. Li, Medium-temperature thermoelectric GeTe: vacancy suppression and band structure engineering leading to high performance, Energy Environ. Sci. **12,** 1396 (2019).

[30] H. Qin, J. Zhu, N. Li, H. Wu, F. Guo, S. Sun, D. Qin, S. J. Pennycook, Q. Zhang, W. Cai, and J. Sui, Enhanced mechanical and thermoelectric properties enabled by hierarchical structure in medium-temperature Sb_2Te_3 based alloys, Nano Energy **78,** 105228 (2020).

[31] B. Lu, M. Wang, J. Yang, H. Hou, X. Zhang, Z. Shi, J. Liu, G. Qiao, and G. Liu, Dense twin and domain boundaries lead to high thermoelectric performance in Sn-doped Cu_3SbS_4, Appl. Phys. Lett. **120,** 173901 (2022).

[32] T. Yue, Y. Sun, Y. Zhao, S. Meng, and Z. Dai, Thermoelectric performance in the binary semiconductor compound A_2Se_2 (A = K, Rb) with host-guest structure, Phys. Rev. B **105,** 054305 (2022).

[33] S. F. Wang, Z. G. Zhang, B. T. Wang, J. R. Zhang, and F. W. Wang, Intrinsic Ultralow Lattice Thermal Conductivity in the Full-Heusler Compound Ba_2AgSb, Phys. Rev. Appl. **17,** 034023 (2022).

[34] W. Cao, Z. Wang, L. Miao, J. Shi, and R. Xiong, Thermoelectric properties of strained β-Cu_2Se, ACS Appl. Mater. Interfaces **13,** 34367 (2021).

[35] L. Yang, Z. G. Chen, G. Han, M. Hong, Y. Zou, and J. Zou, High-performance thermoelectric Cu_2Se nanoplates through nanostructure engineering, Nano Energy **16,** 367 (2015).

[36] B. Koley, A. Lakshan, P. R. Raghuvanshi, C. Singh, A. Bhattacharya, and P. P. Jana, Ultralow lattice thermal conductivity at room temperature in Cu_4TiSe_4, Angew. Chem., Int. Ed. **60,** 9106 (2021).

[37] G. Kresse and J. Furthmüller, Efficient iterative schemes for *ab initio* total-energy calculations using a plane-wave basis set, Phys. Rev. B **54,** 11169 (1996).

[38] J. P. Perdew, K. Burke, and M. Ernzerhof, Generalized Gradient Approximation Made Simple, Phys. Rev. Lett. **77,** 3865 (1996).

[39] S. Baroni, S. De Gironcoli, A. Dal Corso, and P. Giannozzi, Phonons and related crystal properties from density-functional perturbation theory, Rev. Mod. Phys. **73,** 515 (2001).

[40] G. K. Madsen, J. Carrete, and M. J. Verstraete, Bolt*z*TraP2, a program for interpolating band structures and calculating semi-classical transport coefficients, Comput. Phys. Commun. **231,** 140 (2018).

[41] T. Fan and A. R. Oganov, A program for calculating transport properties quickly and accurately, Comput. Phys. Commun. **266,** 108027 (2021).

[42] A. M. Ganose, J. Park, A. Faghaninia, R. Woods-Robinson, K. A. Persson, and A. Jain, Efficient calculation of carrier scattering rates from first principles, Nat. Commun. **12,** 2222 (2021).

[43] G. Casu, A. Bosin, and V. Fiorentini, Efficient thermoelectricity in $Sr_2Nb_2O_7$ with energy-dependent relaxation times, Phys. Rev. Mater. **4,** 075404 (2020).

[44] A. Togo and I. Tanaka, First principles phonon calculations in materials science, Scr. Mater. **108,** 1 (2015).

[45] W. Li, J. Carrete, N. A. Katcho, and N. Mingo, ShengBTE: A solver of the Boltzmann transport equation for phonons, Comput. Phys. Commun. **185,** 1747 (2014).

[46] Z. Han, X. Yang, W. Li, T. Feng, and X. Ruan, Four-Phonon: An extension module to ShengBTE for computing four-phonon scattering rates and thermal conductivity, Comput. Phys. Commun. **270,** 108179 (2022).

[47] H. Fan, H. Wu, L. Lindsay, and Y. Hu, *Ab initio* investigation of single-layer high thermal conductivity boron compounds, Phys. Rev. B **100,** 085420 (2019).

[48] G. Matyszczak, S. Sutuła, P. Jóźwik, K. Krawczyk, and K. Woźniak, Preparation, Crystal Structure Characterization and Prediction, and Study of the Bandgap of Cu_4TiSe_4, Available at SSRN: http://doi.org/10.2139/ssrn.4029692

[49] B. Marfoua and J. Hong, Giant thermoelectric performance of an n-type 2D $GaSe_{0.5}Te_{0.5}$ alloy, J. Mater. Chem. C **9,** 10497 (2021).

[50] C. Kumarasinghe and N. Neophytou, Band alignment and scattering considerations for enhancing the thermoelectric power factor of complex materials: The case of Co-based half-Heusler alloys, Phys. Rev. B **99,** 195202 (2019).

[51] J. Zhang, R. Liu, N. Cheng, Y. Zhang, J. Yang, C. Uher, X. Shi, L. Chen, and W. Zhang, High-performance pseudocubic thermoelectric materials from non-cubic chalcopyrite compounds, Adv. Mater. **26,** 3848 (2014).

[52] Z. Chang, K. Liu, Z. Sun, K. Yuan, S. Cheng, Y. Gao, X. Zhang, C. Shen, H. Zhang, and D. Tang, First-principles investigation of the significant anisotropy and ultrahigh thermoelectric efficiency of a novel two-dimensional $Ga_2I_2S_2$ at room temperature, Int. J. Extreme Manuf. **4,** 025001 (2022).

[53] J. Wen, H. Huang, X. Yu, D. Wang, K. Guo, D. Wan, J. Luo, and J. T. Zhao, Thermoelectric properties of p-type Cu_3VSe_4 with high Seebeck coefficients, J. Alloys Compd. **879,** 160387 (2021).

[54] L. Lindsay, D. A. Broido, and T. L. Reinecke, First-Principles Determination of Ultrahigh Thermal Conductivity of Boron Arsenide: A Competitor for Diamond?, Phys. Rev. Lett. **111,** 025901 (2013).

[55] X. Gu, Y. Wei, X. Yin, B. Li, and R. Yang, Colloquium: Phononic thermal properties of two-dimensional materials, Rev. Mod. Phys. **90,** 041002 (2018).

[56] C. Yu, Y. Hu, J. He, S. Lu, D. Li, and J. Chen, Strong four-phonon scattering in monolayer and hydrogenated bilayer BAs with horizontal mirror symmetry, Appl. Phys. Lett. **120,** 132201 (2022).

[57] Y. Ouyang, C. Yu, J. He, P. Jiang, W. Ren, and J. Chen, Accurate description of high-order phonon anharmonicity and lattice thermal conductivity from molecular dynamics simulations with machine learning potential, Phys. Rev. B **105,** 115202 (2022).

[58] N. K. Ravichandran and D. Broido, Phonon-Phonon Interactions in Strongly Bonded Solids: Selection Rules and Higher-Order Processes, Phys. Rev. X **10,** 021063 (2020).

[59] X. Yang, T. Feng, J. Li, and X. Ruan, Stronger role of four-phonon scattering than three-phonon scattering in thermal conductivity of III-V semiconductors at room temperature, Phys. Rev. B **100,** 245203 (2019).

[60] N. T. Hung, A. R. Nugraha, and R. Saito, Designing high-performance thermoelectrics in two-dimensional tetradymites, Nano Energy **58,** 743 (2019).

[61] N. T. Hung, A. R. Nugraha, and R. Saito, Two-dimensional InSe as a potential thermoelectric material, Appl. Phys. Lett. **111,** 092107 (2017).

[62] P. Z. Jia, J. P. Xie, X. K. Chen, Y. Zhang, X. Yu, Y. J. Zeng, Z. X. Xie, Y. X. Deng, and W. X. Zhou, Recent progress of two-dimensional heterostructures for thermoelectric applications, J. Phys.: Condens. Matter **35,** 073001 (2023).

[63] A. S. Chaves, D. T. Larson, E. Kaxiras, and A. Antonelli, Out-of-plane thermoelectric performance for p-doped GeSe, Phys. Rev. B **105,** 205201 (2022).

[64] K. Imasato, C. Fu, Y. Pan, M. Wood, J. J. Kuo, C. Felser, and G. J. Snyder, Metallic n-type Mg_3Sb_2 single crystals demonstrate the absence of ionized impurity scattering and enhanced thermoelectric performance, Adv. Mater. **32,** 1908218 (2020).

[65] S. Han, Z. Zhou, C. Sheng, R. Hu, H. Yuan, Q. Tang, and H. Liu, Decoupling thermoelectric transport coefficients of Dirac semimetal Na_2AgSb with intrinsically

ultralow lattice thermal conductivity, Mater. Today Phys. **21,** 100560 (2021).

[66] Z. Yang, J. Min, T. Dong, W. Wen, Z. Feng, G. Yang, Y. Yan, and Z. Zeng, Flat phonon modes driven ultralow thermal conductivities in Sr_3AlSb_3 and Ba_3AlSb_3 Zintl compounds, Appl. Phys. Lett. **120,** 142103 (2022).

[67] W. Kim, Strategies for engineering phonon transport in thermoelectrics, J. Mater. Chem. C **3,** 10336 (2015).

[68] Z. K. Ding, Y. J. Zeng, H. Pan, N. Luo, J. Zeng, L. M. Tang, and K. Q. Chen, Edge states of topological acoustic phonons in graphene zigzag nanoribbons, Phys. Rev. B **106,** L121401 (2022).

[69] H. Pan, L. M. Tang, and K. Q. Chen, Quantum mechanical modeling of magnon-phonon scattering heat transport across three-dimensional ferromagnetic/nonmagnetic interfaces, Phys. Rev. B **105,** 064401 (2022).

[70] Z. Liu, X. Yang, B. Zhang, and W. Li, High thermal conductivity of Wurtzite boron arsenide predicted by including four-phonon scattering with machine learning potential, ACS Appl. Mater. Interfaces **13,** 53409 (2021).

[71] Z. Qin, G. Qin, X. Zuo, Z. Xiong, and M. Hu, Orbitally driven low thermal conductivity of monolayer gallium nitride (GaN) with planar honeycomb structure: a comparative study, Nanoscale **9,** 4295 (2017).

[72] Y. Xia, K. Pal, J. He, V. Ozoliņš, and C. Wolverton, Particlelike Phonon Propagation Dominates Ultralow Lattice Thermal Conductivity in Crystalline Tl_3VSe_4, Phys. Rev. Lett. **124,** 065901 (2020).

[73] J. J. Ma, Q. Y. Liu, P. F. Liu, P. Zhang, B. Sanyal, T. Ouyang, and B. T. Wang, Ultralow thermal conductivity and anisotropic thermoelectric performance in layered materials LaMOCh (M = Cu, Ag; Ch = S, Se), Phys. Chem. Chem. Phys. **24,** 21261 (2022).

[74] X. K. Chen, X. Y. Hu, P. Jia, Z. X. Xie, and J. Liu, Tunable anisotropic thermal transport in porous carbon foams: The role of phonon coupling, Int. J. Mech. Sci. **206,** 106576 (2021).

[75] X. K. Chen and K. Q. Chen, Thermal transport of carbon nanomaterials, J. Phys.: Condens. Matter **32,** 153002 (2020).

[76] Q. Liu, J. J. Li, D. Wu, X. Q. Deng, Z. H. Zhang, Z. Q. Fan, and K. Q. Chen, Gate-controlled reversible rectifying behavior investigated in a two-dimensional MoS_2 diode, Phys. Rev. B **104,** 045412 (2021).

[77] X. Dong, T. Chen, G. Liu, L. Xie, G. Zhou, and M. Long, Multifunctional 2D g-C_4N_3/MoS_2 vdW heterostructure-based nanodevices: Spin filtering and gas sensing properties, ACS Sens. **7,** 3450 (2022).

[78] R. Chaurasiya, S. Tyagi, N. Singh, S. Auluck, and A. Dixit, Enhancing thermoelectric properties of Janus WSSe monolayer by inducing strain mediated valley degeneracy, J. Alloys Compd. **855,** 157304 (2021).

[79] S. Karmakar and T. Saha-Dasgupta, High-performance thermoelectric properties of strained two-dimensional tellurium, Phys. Rev. Mater. **5,** 124006 (2021).

[80] Y. Han, J. Y. Yang, and M. Hu, Unusual strain response of thermal transport in dimerized three-dimensional graphene, Nanoscale **10,** 5229 (2018).

[81] T. Ouyang and M. Hu, Competing mechanism driving diverse pressure dependence of thermal conductivity of

X Te (X = Hg, Cd, and Zn), Phys. Rev. B **92,** 235204 (2015).

[82] G. J. Snyder and E. S. Toberer, Complex thermoelectric materials, Nat. Mater. **7,** 105 (2018).

[83] Y. Pei, A. D. LaLonde, N. A. Heinz, X. Shi, S. Iwanaga, H. Wang, L. Chen, and G. J. Snyder, Stabilizing the optimal carrier concentration for high thermoelectric efficiency, Adv. Mater. **23,** 5674 (2011).

[84] Y. Zhang, S. Hao, L. D. Zhao, C. Wolverton, and Z. Zeng, Pressure induced thermoelectric enhancement in SnSe crystals, J. Mater. Chem. A **4,** 12073 (2016).

[85] D. G. Cahill, S. K. Watson, and R. O. Pohl, Lower limit to the thermal conductivity of disordered crystals, Phys. Rev. B **46,** 6131 (1992).

[86] X. Wang, Y. Zhao, S. Zeng, Z. Wang, Y. Chen, and J. Ni, Cubic halide perovskites as potential low thermal conductivity materials: A combined approach of machine learning and first-principles calculations, Phys. Rev. B **105,** 014310 (2022).

[87] J. Zheng, D. Shi, Y. Yang, C. Lin, H. Huang, R. Guo, and B. Huang, Anharmonicity-induced phonon hardening and phonon transport enhancement in crystalline perovskite $BaZrO_3$, Phys. Rev. B **105,** 224303 (2022).

[88] T. Zhang, J. H. Lin, X. L. Zhou, and X. Jia, Stable two-dimensional pentagonal tellurene: A high *ZT* thermoelectric material with a negative Poisson's ratio, Appl. Surf. Sci. **559,** 149851 (2021).

[89] L. Elalfy, D. Music, and M. Hu, Metavalent bonding induced abnormal phonon transport in diamondlike structures: Beyond conventional theory, Phys. Rev. B **103,** 075203 (2021).

[90] H. Yu, L. C. Chen, H. J. Pang, P. F. Qiu, Q. Peng, and X. J. Chen, Temperature-dependent phonon anharmonicity and thermal transport in $CuInTe_2$, Phys. Rev. B **105,** 245204 (2022).

[91] S. Shahabfar and S. S. Naghavi, Mind the mines: Lapieite minerals with ultralow lattice thermal conductivity and high power factor for thermoelectricity, Chem. Mater. **33,** 9393 (2021).

[92] T. A. Manz, Introducing DDEC6 atomic population analysis: Part 3. Comprehensive method to compute bond orders, RSC Adv. **7,** 45552 (2017).

[93] T. A. Manz and N. G. Limas, Introducing DDEC6 atomic population analysis: Part 1. Charge partitioning theory and methodology, RSC Adv. **6,** 47771 (2016).

[94] J. Y. Raty, M. Schumacher, P. Golub, V. L. Deringer, C. Gatti, and M. Wuttig, A quantum-mechanical map for bonding and properties in solids, Adv. Mater. **31,** 1806280 (2019).

[95] M. Al-Fahdi, X. Zhang, and M. Hu, Phonon transport anomaly in metavalent bonded materials: Contradictory to the conventional theory, J. Mater. Sci. **56,** 18534 (2021).

[96] J. Xiao, L. Yang, S. Liu, and G. Liu, In-situ probing the interface electrochemical properties of chalcopyrite modified by amidoxime-dithiocarbamate ester: Implications to flotation mechanism, Miner. Process. Extr. Metall. Rev. (2022).

[97] G. Li, J. He, Q. An, S. I. Morozov, S. Hao, P. Zhai, Q. Zhang, W. A. Goddard III, and G. J. Snyder,

Dramatically reduced lattice thermal conductivity of Mg$_2$Si thermoelectric material from nanotwinning, Acta Mater. **169**, 9 (2019).

[98] W. Li, J. Carrete, G. K. Madsen, and N. Mingo, Influence of the optical-acoustic phonon hybridization on phonon scattering and thermal conductivity, Phys. Rev. B **93**, 205203 (2016).

[99] J. Qi, *et al.*, Dimer rattling mode induced low thermal conductivity in an excellent acoustic conductor, Nat. Commun. **11**, 5197 (2020).

[100] S. Wang, H. Fan, Z. Zhang, L. Sun, J. Chen, N. Yang, Y. Zhou, B. Li, and L. Dai, Resonant phonon modes induced by molecular rotations in α-pentaerythritol crystals, J. Mater. Chem. C **10**, 14431 (2022).

[101] J. Zheng, D. Shi, S. Liu, Y. Yang, C. Lin, Z. Chang, R. Guo, and B. Huang, Effects of high-order anharmonicity on anomalous lattice dynamics and thermal transport in fully filled skutterudite YbFe$_4$Sb$_{12}$, Phys. Rev. Mater. **6**, 093801 (2022).

[102] Y. Xia, V. I. Hegde, K. Pal, X. Hua, D. Gaines, S. Patel, J. He, M. Aykol, and C. Wolverton, Nonperturbative Phonon Scatterings and the Two-Channel Thermal Transport in Tl$_3$VSe$_4$, Phys. Rev. X **10**, 041029 (2020).

[103] T. Tadano and S. Tsuneyuki, Self-consistent phonon calculations of lattice dynamical properties in cubic SrTiO$_3$ with first-principles anharmonic force constants, Phys. Rev. B **92**, 054301 (2015).

[104] T. Tadano and S. Tsuneyuki, Quartic Anharmonicity of Rattlers and Its Effect on Lattice Thermal Conductivity of Clathrates from First Principles, Phys. Rev. Lett. **120**, 105901 (2018).